MOX-Report No. 51/2018

Assessing the disturbed flow and the transition to turbulence in the arteriovenous fistula

Stella, S.; Vergara, C.; Giovannacci, L.; Quarteroni, A.; Prouse, G.

MOX, Dipartimento di Matematica
Politecnico di Milano, Via Bonardi 9 - 20133 Milano (Italy)

mox-dmat@polimi.it http://mox.polimi.it

Assessing the disturbed flow and the transition to turbulence in the arteriovenous fistula

S. Stella[1], C. Vergara[2], L. Giovannacci[1], A. Quarteroni[2], G. Prouse[1]

October 29, 2018

[1] EOC-Ente Ospedaliero Cantonale
Lugano, Switzerland
Via Tesserete 46, 6900 Lugano, Switzerland
<simone.stella,luca.giovannacci,giorgio.prouse>@eoc.ch

[2] MOX– Modellistica e Calcolo Scientifico
Dipartimento di Matematica
Politecnico di Milano
via Bonardi 9, 20133 Milano, Italy
<christian.vergara,alfio.quarteroni>@polimi.it

Keywords: Arteriovenous fistula, Large Eddy simulations, disturbed flow

Abstract

The arteriovenous fistula (AVF) is the main form of vascular access for hemodialysis patients, but its maintenance is very challenging. Its failure is mainly related to intimal hyperplasia, leading to stenosis.

The aim of this work is twofold: i) to perform a computational study for the comparison of the disturbed blood dynamics in different configurations of AVF and ii) to assess the amount of turbulence developed by the specific geometric configuration of AVF.

To this aim, we reconstructed realistic 3D geometries of two patients with a *side-to-end* AVF, performing a parametric study by changing the angle of incidence at the anastomosis. We solved the incompressible Navier-Stokes equations modeling the blood as an incompressible and Newtonian fluid. Large Eddy Simulations (LES) were considered to capture the transition to turbulence developed at the anastomosis. The values of prescribed boundary conditions are obtained from clinical Echo-Color Doppler measurements.

To assess the disturbed flow, we considered hemodynamic quantities such as the velocity field, the pressure distribution, and wall shear stresses derived quantities, whereas to quantify the transition to turbulence, we computed the standard deviation of the velocity field among different heartbeates and the turbulent kinetic energy.

1 Introduction

The arteriovenous fistula (AVF) is currently the main vascular access for patients on hemodialysis. A distal radiocephalic AVF, which is considered the first choice in most patients starting dialysis, consists in connecting the radial artery and the cephalic vein by means of a surgical procedure in order to provide an access for the vein with a suitable "arterial" blood flow. In particular, one of the most used techniques is the *side-to-end* AVF, where the vein is anastomosed onto the artery.

In the literature there is a general consensus on the use and effectiveness of native vessel AVFs over the arteriovenous graft (AVG) [35], the alternative procedure often used to prepare an access for haemodyalisis consisting in connecting the artery and the vein by inserting a synthetic tube.

In 1966 Brescia et al. [10] described for the first time the surgical creation of an AVF to establish a vascular access in hemodialysis patients. Since then, several studies have been performed to investigate the main difficulties related to AVF. In particular, early and late failure could occur [2]. This is mostly due to intimal hyperplasia, i.e. the thickening of the tunica intima in the blood vessel, leading to stenosis and subsequent trombosis. Blood dynamics seems to play a major role in these processes [14,28,29,36]. In particular, regions with disturbed flows could favour the development of conditions that lead to stenosis [32, 38]. Nowadays the failure rate is high, especially in the long term (the mean one-year patency rate), in spite of the presence of clinical guidelines that suggest criteria to create AVF [50].

Computational models are an effective tool to study the disturbed flow in AVF due to its non-invasiveness that allows the analysis of local hemodynamic factors involved in the risk of failure [12,22,30]. In the last twenty years computational fluid dynamics (CFD) was used specifically for the study of AVF to assess the role of Wall Shear Stresses (WSS) and their oscillations in the mechanism of pathogenesis of the intimal hyperplasia [15]. In this context, the transient or turbulent nature that characterizes the flow regime at the anastomosis seems to have a strong impact on CFD quantities increasing the risk of stenosis [31].

The goal of this work is twofold. The first one consists in performing a computational study in two 3D geometries of patients with a side-to-end AVF with the aim of comparing the disturbed blood dynamics for possible configurations of AVF. In particular, we perform a parametric study by changing the angle of incidence at the anstomosis and we model the blood as an incompressible and Newtonian fluid. To capture the transitional effects highlighted in AVF, an eddy viscosity model based on large eddy simulations (LES) is considered in the numerical experiments. The parametric analysis is performed by assessing some postprocessed quantities as a function of the incidence angle. In particular, we show and discuss the distribution of the Oscillatory Shear Index (OSI), the velocity field, and the pressure [34].

The second aim of this work is to evaluate the amount of turbulence that is

generated close to the anastomosis as a consequence of the characteristic shape of the fistula domain. This is of utmost importance from the clinical point of view since the presence of turbulence could be source of instabilities. To evaluate the transitional and turbulent effects we analyze the ratio between eddy and molecular viscosities, the standard deviation of the velocity field over several heartbeats, and the turbulent kinetic energy.

2 Materials and methods

2.1 Geometric data

The geometries of two patients (named in what follows P1 and P2) were reconstructed using data obtained by Echo-Color Doppler (ECD) performed at the EOC-Ente Ospedaliero Cantonale, Lugano, Switzerland, in particular at the Divisions of Vascular Surgery and Angiology. The patients who underwent ECD were selected for inclusion in the present study, which was approved by the ethical review board of the hospital. The incidence angles α at the anastomosis were equal to 40° for P1 and 70° for P2.

3D geometric reconstructions were then performed following two steps. In the first one, starting from the ECD data (angle of the fistula, diameters of the vessels in several points), the Paraview software [5] was used to build the patient-specific external lumen boundary surfaces, see Figure 1.

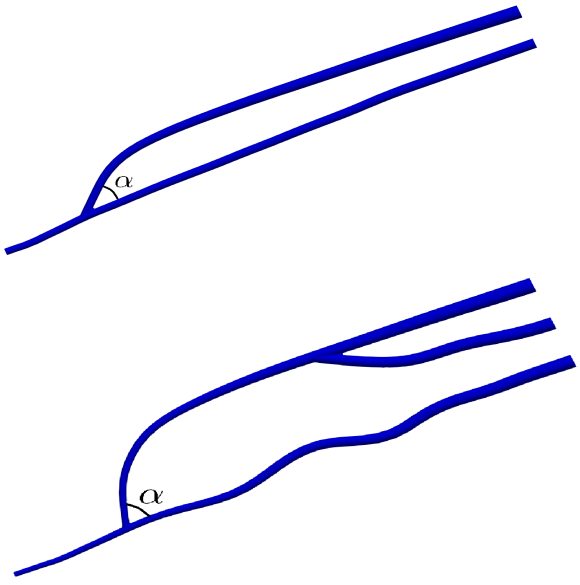

Figure 1: Patient-specific geometries of P1 (top) and P2 (bottom).

Once the lumen surfaces reconstructions of the two patients at hand were

available, we built other two configurations for each patient. In particular, we consider $\alpha = 20°$, $60°$ for P1 and $\alpha = 30°$, $50°$ for P2. The six configurations obtained were named in what follows $P1{-}20$, $P1{-}40$, $P1{-}60$, $P2{-}30$, $P2{-}50$, $P2{-}70$, where the first part of the name refers to the patient and the second to the angle of incidence α.

After the generation of the external surfaces of the fistula and of the inflow and outflow vessels, we used them as an input for the Vascular Modeling Toolkit, VMTK [3], to obtain improved models of the six lumen surfaces. To this aim, a gradient-driven level set technique was considered. Finally, the reconstructions of the internal volumes were performed by turning the external surfaces into volumetric meshes of linear tetrahedra, with three thin layers close to the wall, see Figure 2. In particular, the meshes were formed by 513k (P1-20), 517k (P1-40), 516k (P1-60), 381k (P2-30), 329k (P2-50), 323k (P2-70) tetrahedra. The corresponding characteristic space discretization parameter is about $h = 0.05\ cm$ for all the configurations. These meshes were obtained after a mesh convergence test aiming at finding configurations where the WSS do not change up to a tolerance equal to 4%.

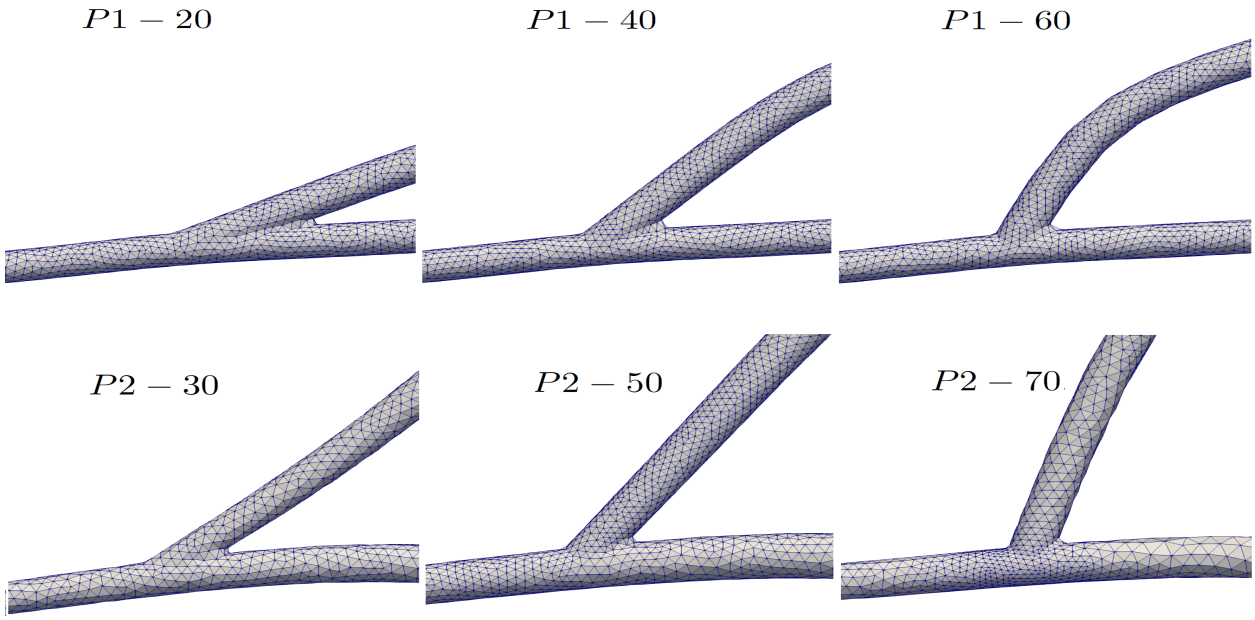

Figure 2: Zoom at the anastomosis of the computational meshes.

2.2 Numerical methods

Blood is modeled as an incompressible Netwonian fluid with constant density, a well accepted hypothesis in medium and large vessels [25]. To capture transition to turbulence, a LES model is considered. In particular, we used the *σ-model*

proposed for the ventricular blood dynamics in [39] and successfully used for stenotic carotids and abdominal aortic aneurysms in [33] and [51], respectivley. LES are based on the decomposition of the fluid unknowns in resolved and unresolved quantities, $[\bar{\boldsymbol{u}}, \bar{p}]$ and $[\boldsymbol{u}', p']$, respectively, so that $\boldsymbol{u} = \bar{\boldsymbol{u}} + \boldsymbol{u}'$ and $p = \bar{p} + p'$ [42]. The resolved quantities are referred to as *filtered*. To derive a set of equations for $\bar{\boldsymbol{u}}$ and $\bar{p}$, a filtering procedure is applied to the Navier-Stokes equations. Referring to Figure 3, we consider the following filtered Navier-Stokes problem (normalized over the fluid density):
For each $t \in (0, NT]$, find the velocity $\bar{\boldsymbol{u}}(t, \boldsymbol{x})$ and the pressure $\bar{p}(t, \boldsymbol{x})$ such that

$$\begin{aligned}
\frac{\partial \bar{\boldsymbol{u}}}{\partial t} - \nu \nabla \cdot \boldsymbol{S}(\bar{\boldsymbol{u}}) + \nabla \cdot (\bar{\boldsymbol{u}} \otimes \bar{\boldsymbol{u}}) + \nabla \bar{p} + \nabla \cdot \boldsymbol{\tau}^d(\bar{\boldsymbol{u}}) &= \boldsymbol{0} \quad \boldsymbol{x} \in \Omega, \qquad \text{(1a)} \\
\nabla \cdot \bar{\boldsymbol{u}} &= 0 \quad \boldsymbol{x} \in \Omega, \\
\bar{\boldsymbol{u}} &= \boldsymbol{g} \quad \boldsymbol{x} \in \Gamma_{in}, \\
-\bar{p}\boldsymbol{n} + \nu \boldsymbol{S}(\bar{\boldsymbol{u}})\boldsymbol{n} - \boldsymbol{\tau}^d(\bar{\boldsymbol{u}})\boldsymbol{n} &= \boldsymbol{0} \quad \boldsymbol{x} \in \Gamma_{out},
\end{aligned}$$

with a suitable initial condition, and where $(\boldsymbol{v} \otimes \boldsymbol{v})_{ij} = v_i v_j$, $\boldsymbol{S}(\boldsymbol{v}) = \nabla \boldsymbol{v} + (\nabla \boldsymbol{v})^T$, $\Gamma_{in} \cup \Gamma_{out} = \partial\Omega$, $\Gamma_{in} \cap \Gamma_{out} = \emptyset$, with Γ_{in} and Γ_{out} partitions of $\partial\Omega$ where Dirichlet and Neumann boundary conditions are prescribed, respectively; moreover, ν is the kinematic viscosity, $\boldsymbol{g}(t, \boldsymbol{x})$ is a given velocity boundary data, N is the number of heartbeats and T the period of a heartbeat. Notice that the Dirichlet boundary Γ_{in} coincides with the arterial extremities and it is split into two parts, $\Gamma_{in,up}$ and $\Gamma_{in,down}$. The datum $\boldsymbol{g}$ has been obtained by considering at each time step a parabolic spatial profile over the largest circle inscribed in the arterial boundaries fitting the flow rates $Q_{up}(t)$ and $Q_{down}(t)$. These data have been obtained as follows: the waveforms of the two signals, depicted in Figure 4, has been taken from [23] as representative of the flow rates in the systemic and distal part of the artery in AVF. They are the same for both the patients. The intensity of such signals have been instead tuned owing to patient-specific measures of the average flow rates $\overline{Q}_{up}$ and $\overline{Q}_{down}$ over a heartbeat obtained by means of ECD measures. In particular, we have the following data: $\overline{Q}_{up} = 8.0\, cm^3/s$ and $\overline{Q}_{down} = 1.0\, cm^3/s$ for P1 and $\overline{Q}_{up} = 8.5\, cm^3/s$ and $\overline{Q}_{down} = 0.4\, cm^3/s$ for P2. Notice also that the Neumann boundary Γ_{out} coincides with the venous extremity where an homogenous traction condition is prescribed.

In (1), we have introduced $\boldsymbol{\tau}^d$, the deviatoric part of $\boldsymbol{\tau}$, which is the subgrid-scale tensor defined as

$$\boldsymbol{\tau} = \overline{\boldsymbol{u} \otimes \boldsymbol{u}} - \bar{\boldsymbol{u}} \otimes \bar{\boldsymbol{u}},$$

which models the effect of the (smallest) unresolved scales on the resolved ones [40,45]. The choice of the subgrid-scale tensor $\boldsymbol{\tau}$ (or better of its deviatoric part) characterizes the LES model. In this work, we consider an *eddy viscosity* model, were a subgrid-scale viscosity ν_{sgs} is introduced allowing to model the deviatoric part of the subgrid-scale tensor as $\boldsymbol{\tau}^d = -2\nu_{sgs}(\bar{\boldsymbol{u}})\boldsymbol{S}(\bar{\boldsymbol{u}})$. In particular, we use

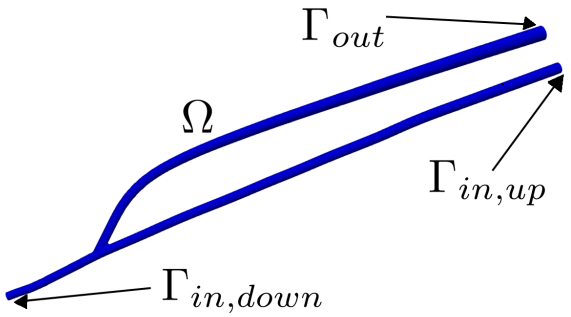

Figure 3: Computational domain for the fistula geometry.

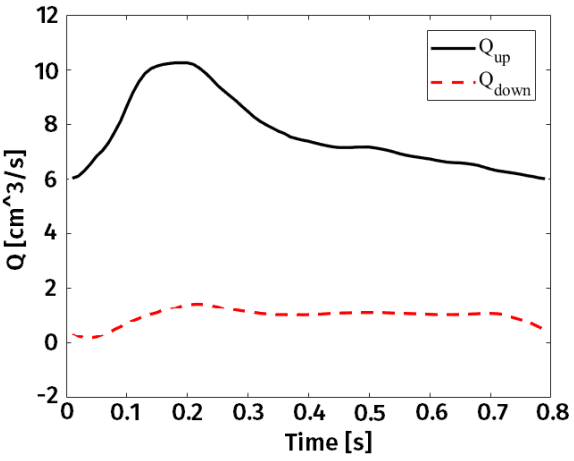

Figure 4: Flow waveform measured with ECD and prescribed at the arterial boundaries. The values reported correspond to P1.

the so-called σ-model [39, 51], where the subgrid viscosity is given by

$$\nu_{sgs} = C\bar{\Delta}^2 \frac{\sigma_3(\sigma_1 - \sigma_2)(\sigma_2 - \sigma_3)}{\sigma_1^2},$$

with $\sigma_1(t, \boldsymbol{x}) \geq \sigma_2(t, \boldsymbol{x}) \geq \sigma_3(t, \boldsymbol{x}) \geq 0$ the singular values of $\nabla \bar{\boldsymbol{u}}$, C a suitable constant, and $\bar{\Delta}$ the filter width. For our simulations we used $C = 1.5$ [33,39,51]. For the grid filter we considered an *implicit* procedure [17], where the filter width $\bar{\Delta}$ represents the size of the mesh.

For the time discretization, we use a semi-implicit approach to linearize the momentum equation (1a), used in combination with a backward differentiation formula of order 2 (BDF2) [26]. The convective field and the subgrid-scale viscosity have been extrapolated by previous time steps with a second order formula. This choice leads to a CFL-like condition on the time step Δt ($\Delta t \lesssim h$ [41]). For the space discretization we use Finite Elements with a SUPG stabilization term to control numerical instabilities due to the large convective term [49]. We used $P2$-$P2$ finite elements for the approximation of the pressure and each velocity component. Furthermore a Pressure Stabilized Petrov-Galerkin (PSPG) formulation [49] was used to guarantee well-posedness of the discrete problem.

We use the following data: kinematic viscosity $\nu = 0.035\ cm^2/s$, time step $\Delta t = 0.01\ s$, number of hearthbeats $N = 4$, and hearthbeat period $T = 0.8\ s$.

All numerical results have been obtained using the parallel Finite Element library *LifeV* (https://bitbucket.org/lifev-dev/lifev-release/wiki/Home).

2.3 Quantities of interest

To describe the blood dynamics in the fistulae in order to compare the different configurations, we introduce the following post-processed quantities, which will give useful indications about risk of restenosis:

- *Ensemble-average.* Given a quantity $q(t, \boldsymbol{x})$, we define its ensemble-average as

$$< q(t, \boldsymbol{x}) >= \frac{1}{N} \sum_{i=1}^{N} q(t + (i-1)T, \boldsymbol{x}), \quad t \in (0, T].$$

  This allows us to remove from the field of interest the random fluctuations due to the transitional effects appearing at each heartbeat. In particular, we consider the ensemble-average velocity magnitude $< U >$, pressure $< p >$, and wall shear stress $< WSS >$, where

$$U(t, \boldsymbol{x}) = \|\bar{\boldsymbol{u}}(t, \boldsymbol{x})\|_{\mathbb{R}^3}, \qquad t \in (0, NT],$$

$$WSS(t, \boldsymbol{x}) = \nu \sqrt{\sum_{i=1}^{2} ((\nabla \bar{\boldsymbol{u}}\, \boldsymbol{n}) \cdot \boldsymbol{\tau}^{(i)})^2}, \qquad t \in (0, NT].$$

  The latter quantity is computed on the lateral surface, where $\boldsymbol{n}$ is the outward unit vector and $\boldsymbol{\tau}^{(j)}$, $j = 1, 2$, the tangential unit vectors;

- *Standard deviation of the fluctuations of the velocity magnitude.* This is defined as

$$SD(t,\boldsymbol{x}) = \sqrt{\frac{1}{N}\sum_{i=1}^{N}(U(t+(i-1))T,\boldsymbol{x}) - < U(t,\boldsymbol{x}) >)^2}, \quad t \in (0,T].$$

This allows us to quantify and localize the velocity fluctuations among the heartbeats.

- *Oscillatory Shear Index.* This is defined as

$$OSI(\boldsymbol{x}) = \frac{1}{2}\left(1 - \frac{\| \int_0^T < WSS(t,\boldsymbol{x}) > dt \|}{\int_0^T \| < WSS(t,\boldsymbol{x}) > \| dt}\right).$$

This allows us to quantify the oscillatory nature of the WSS which is known to be highly correlated with stenosis development [32, 38, 46].

- *Relative Residence Time.* This quantity is defined as

$$RRT(\boldsymbol{x}) = \frac{1}{(1-2OSI(\boldsymbol{x}))TAWSS(\boldsymbol{x})},$$

where $TAWSS(\boldsymbol{x}) = \frac{1}{T}\int_0^T \| < WSS(t,\boldsymbol{x}) > \| dt$ is the *Time Averaged WSS*. RRT is considered as an effective metric of low and/or oscillatory WSS [46]. It has been used by many authors to localize the regions at risk of stenosis [7, 34].

- *Global Turbulent Kinetic Energy.* Given the Turbulent Kinetic Energy $TKE(t,\boldsymbol{x})$, defined as follows [37]

$$\begin{aligned} TKE(t,\boldsymbol{x}) = \frac{1}{2N}\sum_{j=1}^{N}\Big(& (\bar{u}_x(t+(j-1)T,\boldsymbol{x}) - < u_x(t,\boldsymbol{x}) >)^2 + \\ & + (\bar{u}_y(t+(j-1)T,\boldsymbol{x}) - < u_y(t,\boldsymbol{x}) >)^2 + \\ & + (\bar{u}_z(t+(j-1)T,\boldsymbol{x}) - < u_z(t,\boldsymbol{x}) >)^2 \Big), \\ & t \in (0,T], \end{aligned}$$

we define the *Global Turbulent Kinetic Energy* as the space integral of $TKE(t,\boldsymbol{x})$ [51]:

$$GTKE(t) = \int_\Omega TKE(t,\boldsymbol{x})d\boldsymbol{x}, \quad t \in (0,T].$$

$GTKE(t)$ allows us to identify the instants where (in average) high velocity fluctuations occur.

3 Results

In this section we report some numerical results obtained in the different scenarios with the aim of assessing the influence of the angle of incidence on the formation of distrubed flows and transition to turbulence, that could play a major role in intimal hyperplasia development.

In Figure 5 we report for all the computational scenarios the velocity magnitude during the fourth heartbeat on a selected region together with the streamlines to describe the flow direction in the fistula. From these results we can observe that the flow is characterized by two jets (one coming from the proximal artery inlet $\Gamma_{in,up}$ and the other one coming from the distal artery inlet $\Gamma_{in,down}$, see Figure 3) that collide at the fistula and deviate towards the vein. The flow in the proximal artery is bigger than the distal one and, as expected, we can observe that the fistula works as a bend for the main flow direction. It is also possible to notice the presence of vortices (of different magnitude, depending on the angle of incidence) developed at the anastomosis at different instants of the heatbeat.

In Figure 6 we report the ensamble-averaged pressure on a selected longitudinal section. We can observe that increasing the angle, the ensamble-averaged pressure in the artery and at the anastomosis increases during the acceleration and systolic phases, whereas it features comparable values at the deceleration phase. On the other hand, pressure in the vein is characterized by lower (negative) values and seems to be almost independent of the angle of incidence. This implies a greater pressure gradient between artery and vein for elevated values of the incidence angle.

In Figure 7 we report the spatial distribution of OSI computed on ensamble-averaged WSS values. We observe that increasing the incidence angle, the area with higher values of OSI moves from the fistula towards the distal artery. Moreover, for the three angles, the intensity of OSI decreases when the angle increases. This is also confirmed by the values reported in Table 1, where the percentage of area (over the total area in a region of interest) $\%A_{OSI}$ with OSI above the threshold of 0.3 is shown. The value of the threshold used in this analysis has been chosen as representative to discriminate high and small values of OSI. However, the analysis performed with other thresholds brings to the same qualitative conclusions (percentage of area above the threshold increases for decreasing values of the angle).

In the same figure, we also reported the spatial distribution of RRT computed on ensamble-averaged WSS values. We observe again the shifting of the region with elevated values towards the distal artery when the angle is increased. In Table 2, we report the percentage of area (over the total area in a region of interest) $\%A_{RRT}$ with RRT above the threshold of 2.5 Pa^{-1}. Again, we notice that the area exposed to "high" values of RRT increases for decreasing values of the angle and that this qualitative trend is independent of the threshold.

In Figure 8 we report the values of the standard deviation (SD) of the ve-

Angle	20/30	40/50	60/70
P1	16.6%	10.8%	8.1%
P2	26.9%	14.6%	9.3%

Table 1: Percentage of area $\%A_{OSI}$ over the total area in a region of interest with OSI above the threshold of 0.3.

Angle	20/30	40/50	60/70
P1	32.5%	24.3%	21.6%
P2	29.9%	23.3%	21.7%

Table 2: Percentage of area $\%A_{RRT}$ over the total area in a region of interest with RRT above the threshold of 2.5 Pa^{-1}.

locity magnitude over 4 heartbeats at the same selected longitudinal section and instants as for the pressure analysis. This allows to quantify the variability of the velocity field over different heartbeats and thus the possible presence of transition to turbulence effects. We can observe significant values of the velocity standard deviation for all the configurations that match up to about 40% of the velocity values (refer to Figure 5). In particular, SD is noticeable, as expected, at the anastomosis region where transitional effects should arise as a consequence of the jets collision.

In Figure 9 the ratio between subgrid-scale and molecular viscosities on the same section is reported at the mid-deceleration phase. This quantity allows us to quantify how much turbulence (LES) model is active and to identify the regions and the instants of maximum activation. From these results, we can observe that the LES model is mainly active at the anastomosis region, with values of the subgrid-scale viscosity up to eight times greater than those of the molecular viscosity.

In Figure 10 we report the evolution in time of the Global Turbulent Kinetic Energy for both patients P1 and P2. We notice that, especially for P2, the greater angle seems to be characterized by the lowest amount of GTKE. This is confirmed by the results in Table 3, where the mean values of $GTKE(t)$ are reported. Increasing the angle this value decreases, suggesting a low turbulent kinetic energy developed for the highest angle.

Angle	20/30	40/50	60/70
P1	0.069	0.074	0.066
P2	0.095	0.091	0.083

Table 3: Mean values of GTKE ($mJ \cdot s$) over time.

4 Discussion

4.1 Intimal hyperplasia and hemodynamic parameters

The arteriovenous fistula failure is mainly due to stenosis, which can ultimately lead to thrombisis of the access. Stenosis is provoked by a fibro-muscular thickening of the vessel, the so-called intimal hyperplasia (IH) [43]. It has been found that failure of AVF ranges from 30% to 50% [19]. Among them, the majority of AVF fail because of IH [9].

One of the main factors that triggers IH is the wall shear stress exerted by the blood on the endothelium [27]. In particular, low and oscillatory WSS should create the conditions that facilitate IH development [23,36,38]. Also flow instabilities and turbulence at the anastomosis might be responsible for IH [30].

In the present work we performed a Computational Fluid Dynamics study of the hemodynamics in two arteriovenous fistulae of patients from EOC-Ente Ospedaliero Cantonale, Lugano, Switzerland. The study has been approved by the Ethics Committee of the hospital according to institutional ethics guidelines. All the patients gave a written consent for the publication of data.

The aim of this study was to compute hemodynamic parameters such as WSS and GTKE which are not directly measurable by clinicians. In particular, we performed a parametric study to investigate which are the angles of incidence between the venous and the arterial tracts that guarantee better hemodynamic conditions in terms of reduced disturbed flow and transition to turbulence.

4.2 Overview of computational studies and discussion of the proposed method

Since 1966, when the first AVF was accomplished by Brescia and colleagues [10], several numerical studies were performed to assess the role of the AVF in hemodialysis patients and its risk of failure.

Exploiting the fact that the configuration given by artery and vein with the fistula is easily represented by straight channels, some authors considered ideal computational geometries for their numerical simulations [11,12,23,48]. On the other hand, in order to obtain more physiological results, other authors, as done in the present study, performed numerical studies in realistic AVF geometries [13,24,28,30].

Concerning the blood rheology, most of the studies considered a Newtonian behaviour justified by the dimensions of the vessels involved in the fistula which are large enough to neglect the effect of the cells. However, a non-Newtonian behaviour has been also considered in [8,24]. In our study we decided to assume the blood as a Newtonian fluid, in accordance with the results obtained in [1] where it is shown that non-Newtonian effects compared with the Newtonian ones in the fistula are almost negligible.

In order to study the influence of the vessel wall displacement, some authors performed fluid structure interaction (FSI) simulations in AVF [16, 18] high-

lighting that some differences between the FSI and the rigid model occur. In particular, they found an overestimation of about 10% of WSS when rigid walls are considered. However, as a first study, we decided here to assume rigid walls. We believe that possible inaccuracies introduced by this hypothesis should not influence too much the conclusions of the results we will discuss in the next two sections, which are mainly focused on the comparison between different scenarios, all affected by the same approximation. However, we have in mind to account for future works for the vessel wall displacement, focusing in particular on the mismatch between the vein and the artery wall rigidity, which should play an important role in the hemodynamic effects in the fistula.

Regarding the analysis of turbulence and/or transitional effects in the AVF, a few works have included turbulence models in their simulations. The $k-\omega$ model was considered e.g. in [48] to show how an adjustable band works on the fistula. In [11], the blood dynamics in an arteriovenous junction was studied considering a LES model, specifically the dynamic Smagorinsky model, however without providing an analysis of the results in terms of turbulence developed at the anastomosis. In this study, we considered a LES model, in particular the static σ-model, to reduce significantly the computational cost of the simulations allowing us to use a coarser mesh with respect to the one needed by a DNS, but still able to capture transitional effects. Notice that we considered a second order finite elements approximation, thus the "effective" mesh size to be compared with a DNS one is $h = 0.025\, cm$.

As observed, our work is a parametric study where hemodynamic conditions that have a clinical impact in AVF failure are compared when the incidence angle at the anastomosis is varied. The first parametric study for AVF has been reported in [12], where the authors change the size of the anastomosis and the angle of incidence in an ideal geometry of AVF. In this pioneering analysis, the authors considered rigid walls and steady and laminar conditions, and performed numerical simulations with the aim of describing the flow distribution, the pressure drop and how they may vary when the anastomosis area and the incidence angle change. We mention also [20] where the authors consider a similar study in ideal geometries also for the case of antegrade flow. The principal innovations of the paper consist in considering pulsatile inlet conditions and in the introduction of the analysis of WSS derived quantities to assess the clinical impact of the change of incidence angle. To better capture the blood dynamic behaviour in AVF, in addition to the analysis reported in [12] and [21], in our work we considered patient-specific geometries and boundary conditions and a turbulence model in pulsatile conditions. As in [21], we focused on the clinical impact that the change of incidence angle may have by analysing the WSS derived quantity OSI. Moreover, to the best of our knowledge, we tried to quantify for the first time the amount of turbulence developed at the anastomosis.

Finally, we conclude this section by noting that in literature there is a general consensus about the hemodynamic quantities able to give useful information about the function of the AVF and in particular its risk of failure. Hemodynamic

quantities that were considered are the velocity field, the pressure distribution, and the wall shear stress (WSS) [8, 13, 23]. Also derived quantities such as OSI are considered as relevant parameters to identify the risk of stenosis for the AVF [8, 24].

4.3 Analysis of the disturbed flow

Our computational study highlighted significant differences in the hemodynamic quantities when the angle of incidence varies in AVF. Thus, from the clinical point of view, the choice of this angle during the surgical procedure of the AVF anastomosis is of great importance to obtain optimal performance and reduce the risk of failure.

In particular, from our analysis the angles that seem to feature the best performance in terms of reduced risk of failure are the largest ones, i.e. $\alpha = 60^\circ$ and $\alpha = 70^\circ$ for the first and the second patient, respectively. As previously mentioned, there is a general consensus in literature regarding the fact that OSI is relevant to identify the risk of IH formation [8, 24]. In accordance with this hypothesis we can observe from Figure 7 and Table 1 that in both patients, by increasing the angle of incidence of the fistula, the area with high values of OSI decreases, thus suggesting a reduced risk of failure. We observe that the percentage of area with high OSI values featured by the largest angles are about 60% (P1) and 40% (P2) smaller than the percentage of the corresponding areas for the smallest angles.

Observing Figure 7 we can also notice that the area with higher values of OSI moves from the anastomosis to the distal artery when the incidence angle is increased. This means that for large values of the angles, the region more prone to stenosis development covers a segment of the radial artery distal to the anastomosis. In our clinical experience though, a stenosis of this segment rarely causes a distal AVF to fail, probably because the most of the flow is coming from the proximal segment. Despite arterial stenoses is less frequent than venous ones [6, 23], some studies reported that these stenoses can reach up to 35% of the total cases [4, 44]. However, in AVF, months after the surgery, the artery undergoes remodelling, which can create outflow veins with changed curvature and in this case the OSI value in that area can increase [23].

From the same figure we have also noticed a similar behaviour for RRT. However, we notice that the localization of high RRT values is more shifted towards the segment of the artery distal to the anastomosis in comparison to OSI. Thus, from RRT it seems that the region at risk could be the distal segment of the artery rather than the anastomosis as suggested by OSI. This is because WSS is very low (almost zero) in the distal artery.

Furthermore, observing Figure 5 we can notice greater values of the local velocity at the anastomosis when the angle of incidence is increased. More specifically, decreasing the angle of incidence the fistula seems to act as a brake, slowing down the flow of the blood. This is in accordance with the OSI values,

since high local velocities aligned with the axial direction prevent stagnation regions and thus allow to maintain elevated values of the wall sheart stress (and thus small OSI). This is also confirmed by the large vortices appearing at the anastomosis for the two smaller angles.

Analyzing Figure 6, we observe that during the heartbeat higher values of the pressure gradient between artery and vein are reached at the peak instant, as expected. These values increase when the incidence angle becomes greater. We notice that high pressure gradients are needed to have elevated local velocities and to maintain the flow aligned with the axial direction, thus preventing recirculation regions. Hence, to prevent high values of OSI and RRT and have a reduced risk of IH development there is the need of elevated pressure gradients between artery and vein that prevent the formation of vortices that dissipate the energy. This is what happens for the highest angles.

We notice that our output seems to be in contradiction with that suggested by the results obtained in [21], where the configuration that minimizes the oscillatory nature of WSS is found to be that with the smallest angle. This discrepancy could be justified by noticing that the ratio between the proximal and distal arterial flow rates prescribed as boundary conditions is very different in the two papers. In particular, this ratio is equal to 2.3 for [21], whereas to 8.0 (P1) and 21.0 (P2) in our study, where the flow rates, unlike in [21], come from patient-specific measures (see Section 2.2). As observed by the results, this implies that the region of collision between the two jets moves towards the distal artery in our case, whereas it is located at the anastomosis for [21]. Probably, this has an effect on the energy needed by the flow coming from the proximal artery to suddenly change its direction, canalising into the vein.

4.4 Analysis of the transitional effects

Talking about turbulence in the fistula is not appropriate, because the pulsatility of the blood flow causes instabilities and at the same time does not allow the complete development of the flow into the turbulent regime. For this reason, we prefer to refer to instabilities as transition to turbulence. In any case, the analysis of transitional effects in AVF is of great importance since, as observed, flow instabilities at the anastomosis could increase the risk of IH [31].

The presence of transitional effects in AVF is well documented by several experiments that measured significant wall vibrations [47], as well as by the surgeons who experience a palpable thrill and an audible murmur.

According to the previous observations, in this work we decided to include a turbulence model and to assess, at the best of our knowledge for the first time, a detailed quantification of the transitional effects in AVF, by analyzing the velocity standard deviation, the ratio between the subgrid-scale and molecular viscosities, and the Global Turbulent Kinetic Energy.

First, we notice that the presence of transitional effects in the fistula is significant at the anastomosis, independently of the angle of incidence. This is

noticed by Figure 8, where large values of the standard deviation of the velocity magnitude are present (about 40% of the velocity magnitude).

As a further analysis of the turbulence effects we computed GTKE (see Figure 10 and Table 3). From these results we observed that the amount of transition to turbulence seems to be reduced for the highest angle. Thus, also these results suggest that the highest angle seems to be the most promising choice from the clinical point of view.

Regarding the turbulence model, the suitability of the LES σ-model, is confirmed by Figure 9, where we can observe that, for both patients and all angles considered, the regions with high values of the subgrid-scale viscosity are those of disturbed flow, where high values of the standard deviation of the velocity magnitude occur. Notice that the σ-LES model is active only where needed, in particular at the anastomosis. The use of LES models was made to to enable the simulations to accurately describe turbulent flows on a coarser mesh than the one needed to perform a Direct Numerical Simulation (DNS), where a very high level of refinement is needed to resolve all the scales of motions.

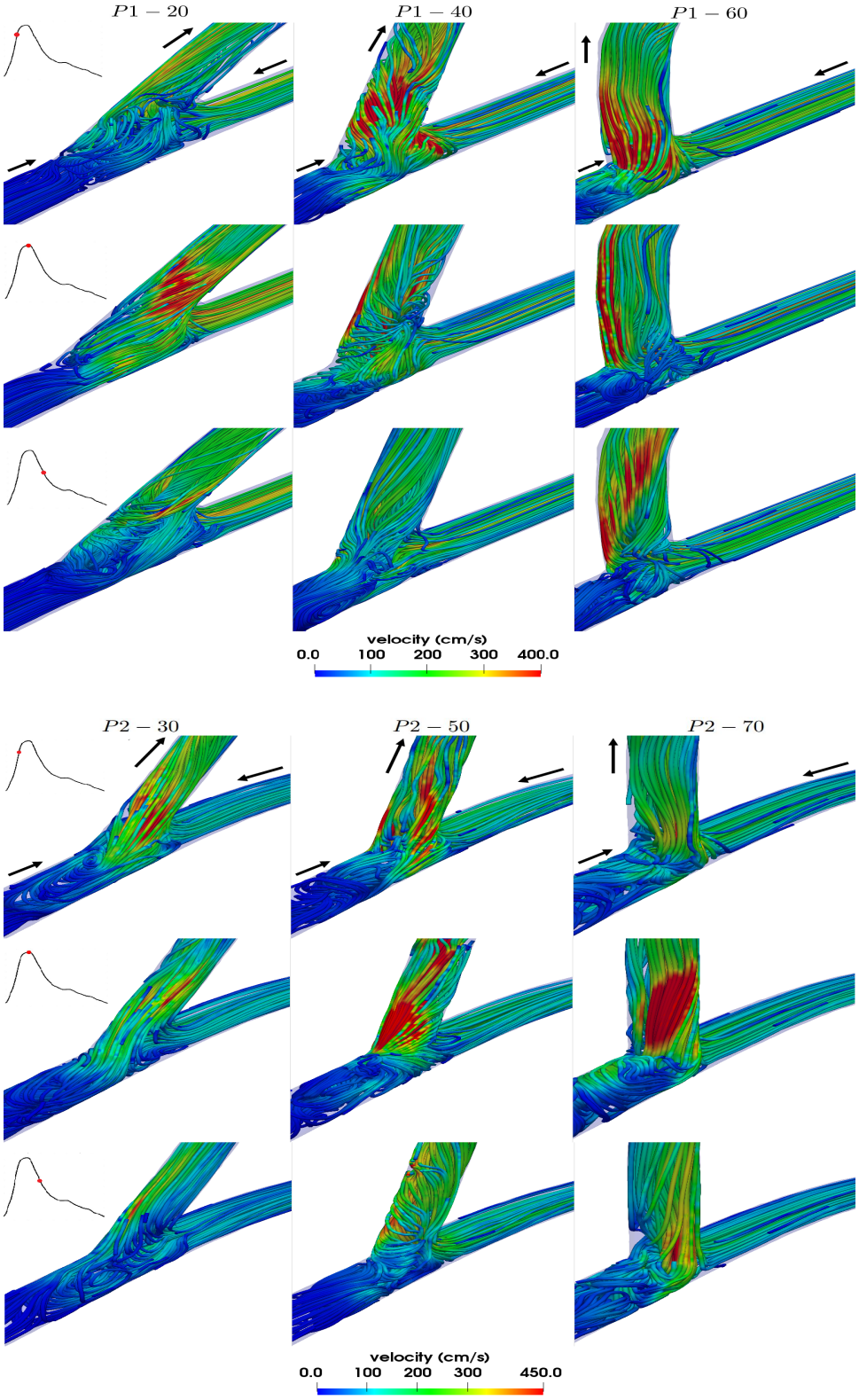

Figure 5: Velocity magnitude on streamlines during the fourth cardiac cycle on a selected region for P1 (top) and P2 (bottom) at three instants over the heartbeat: Acceleration instant $t = 0.12\,s$; Systolic Peak $t = 0.2\,s$; Mid-deceleration $t = 0.30\,s$. For the plots at the acceleration instants, small arrows indicating the main direction of the flow are depicted.

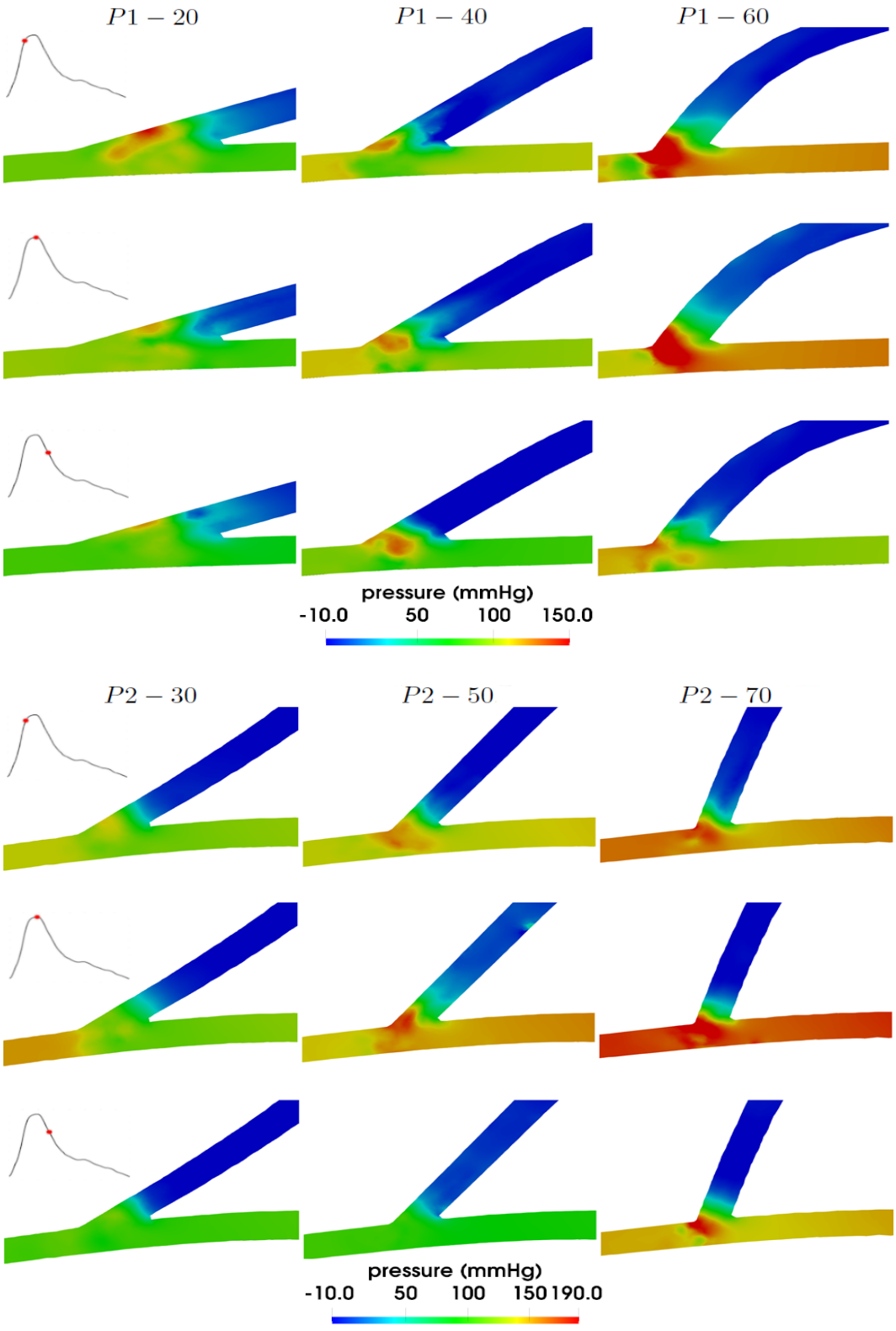

Figure 6: Ensemble-averaged pressure over 4 heartbeats on a selected section for P1 (top) and P2 (bottom) at three instants over the heartbeat: Acceleration instant $t = 0.14\,s$; Systolic Peak $t = 0.2\,s$; Mid-deceleration $t = 0.28\,s$.

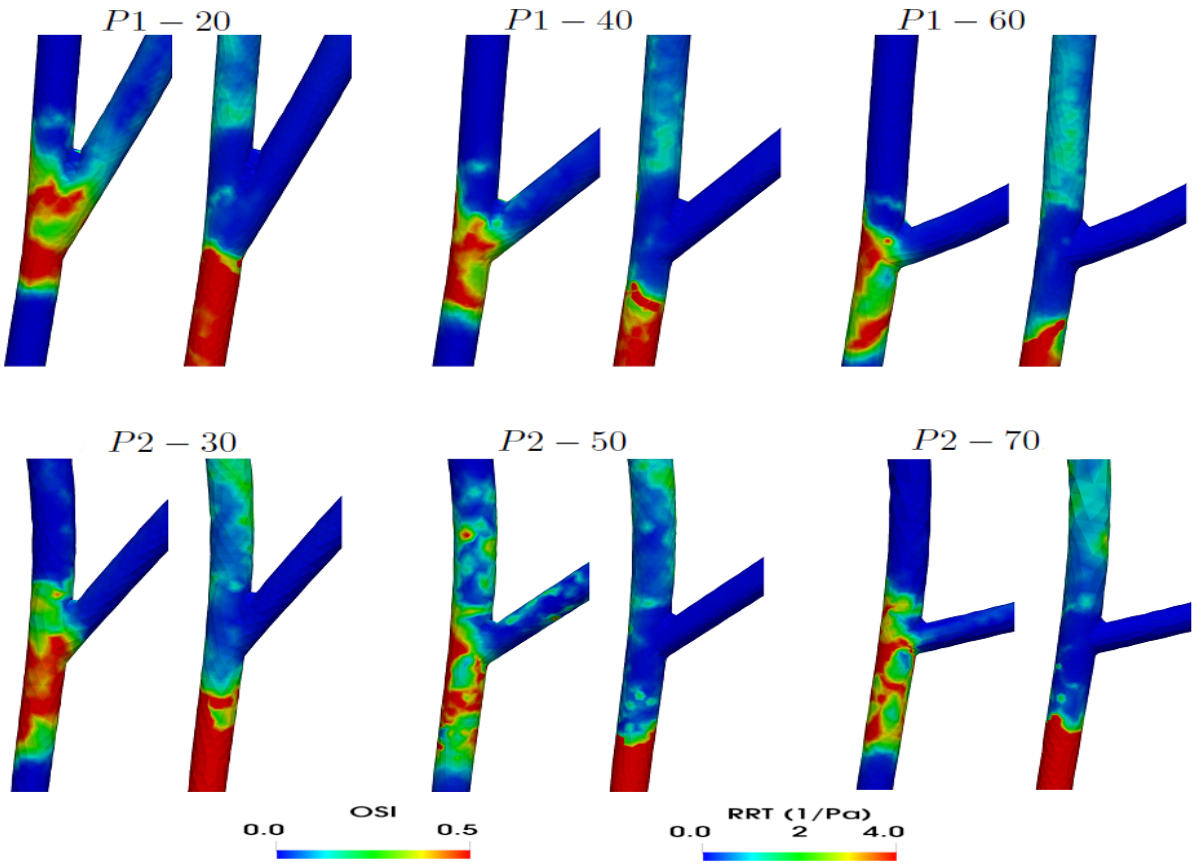

Figure 7: For each box, OSI (left) and RRT (right) at the anastomosis (P1, top; P2, bottom).

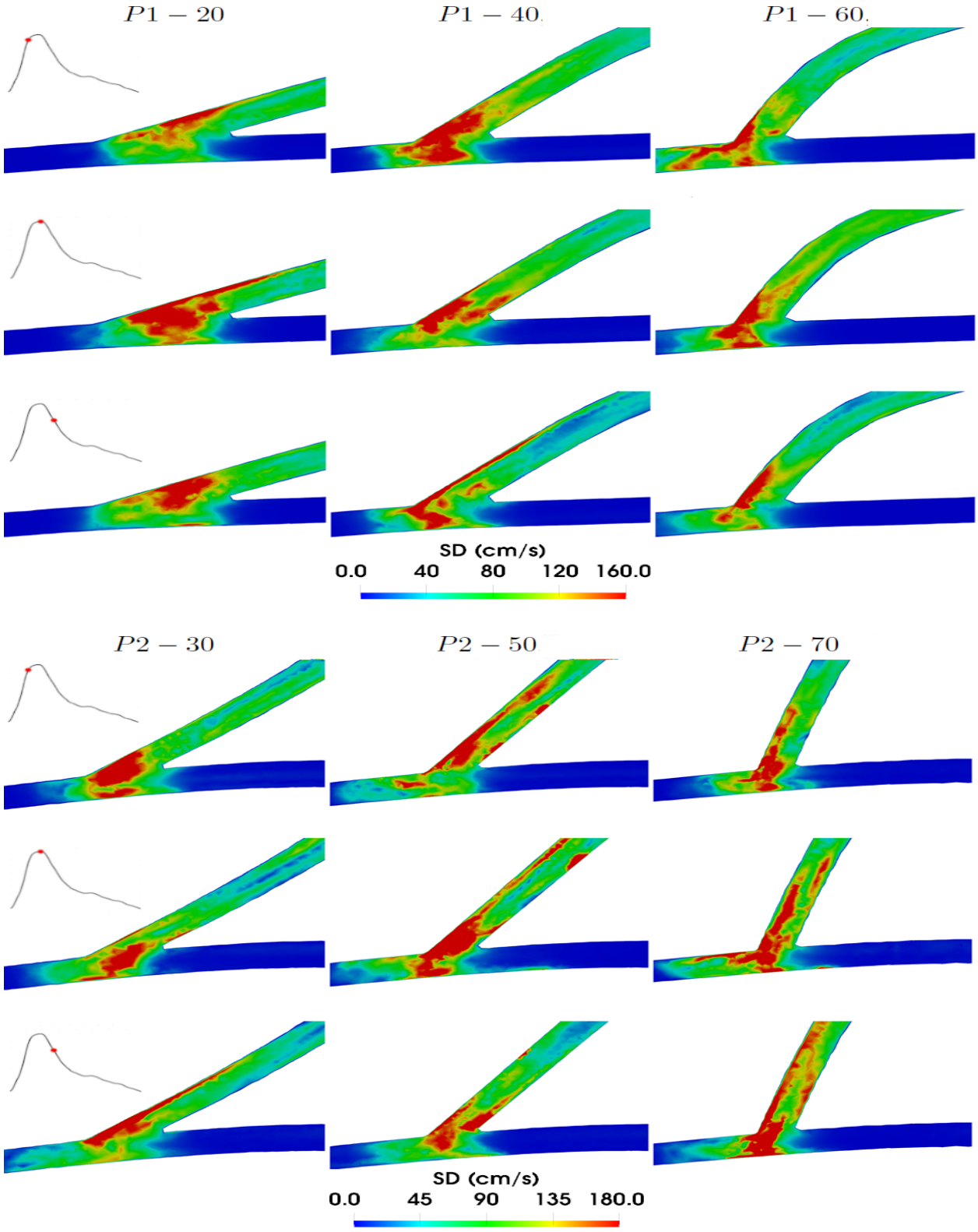

Figure 8: Standard deviation of the velocity magnitude over 4 heartbeats on a selected section for P1 (top) and P2 (bottom) at three instants over the heartbeat: Acceleration instant $t = 0.14\,s$; Systolic Peak $t = 0.2\,s$; Mid-deceleration $t = 0.28\,s$.

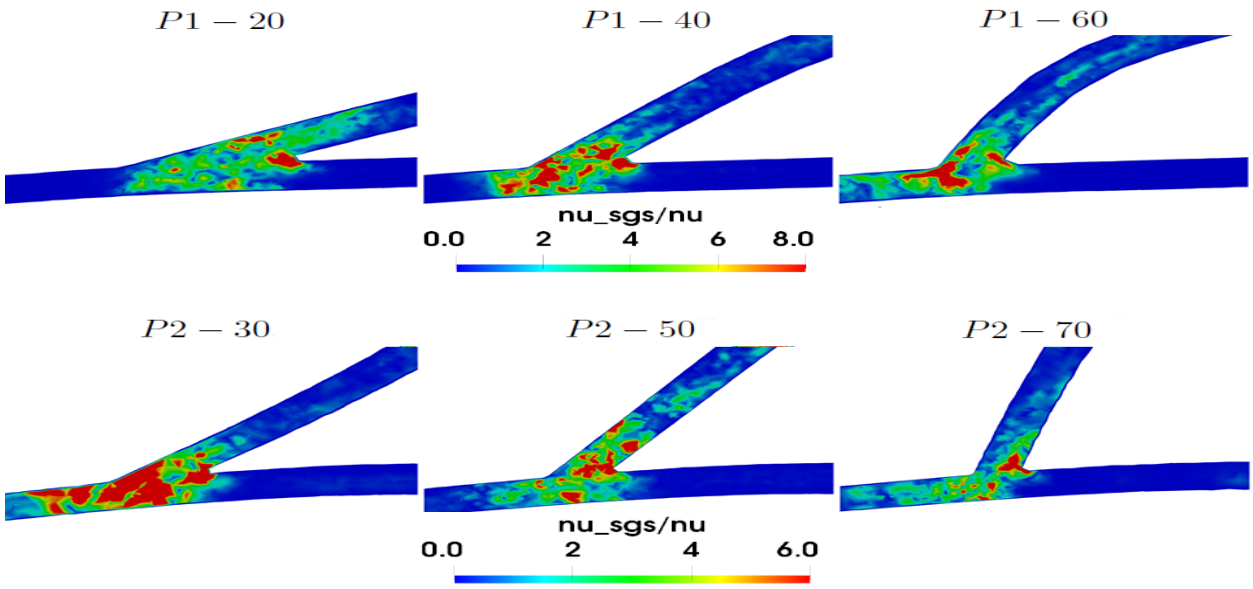

Figure 9: Ratio between subgrid-scale and molecular viscosities on a selected section over 4 heartbeats for P1 (top) and P2 (bottom) at the mid-deceleration instant $t = 0.28\,s$.

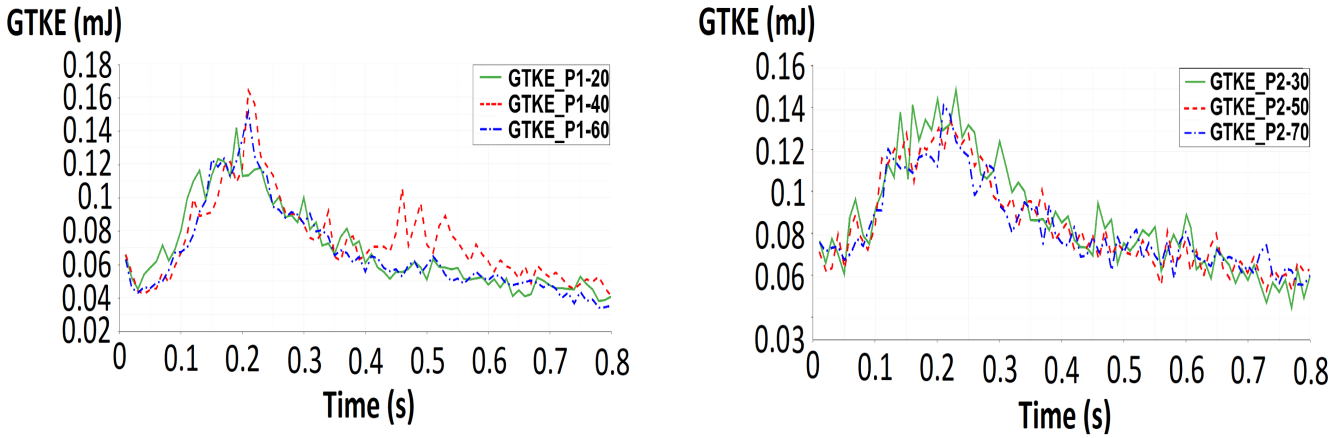

Figure 10: Global Turbulent Kinetic Energy over four heartbeats for P1 (left) and P2 (right).

References

[1] S.M. Javid Mahmoudzadeh Akherat, K. Cassel, M. Boghosian, P. Dhar, and M. Hammes. Are non-newtonian effects important in hemodynamic simulations of patients with autogenous fistula? *Journal of Biomechanical Engineering*, 139(4):044504, mar 2017.

[2] M. Allon and M.L. Robbin. Increasing arteriovenous fistulas in hemodialysis patients: Problems and solutions. *Kidney International*, 62(4):1109–1124, 2002.

[3] L. Antiga and D. Steinman. The vascular modeling toolkit (vmtk), www.vmtk.org. 2009.

[4] A. Asif, F.N. Gadalean, D. Merrill, G. Cherla, C.D. Cipleu, D.L. Epstein, and D. Roth. Inflow stenosis in arteriovenous fistulas and grafts: A multicenter, prospective study. *Kidney International*, 67(5):1986–1992, may 2005.

[5] U. Ayachit. The paraview guide: A parallel visualization application, www.paraview.org. *Kitware*, 2015.

[6] O.J. Badero, M.O. Salifu, H. Wasse, and J. Work. Frequency of swing-segment stenosis in referred dialysis patients with angiographically documented lesions. *American Journal of Kidney Diseases*, 51(1):93–98, jan 2008.

[7] H. S. Bassiouny, S. White, S. Glagov, E. Choi, D.P. Giddens, and C.K. Zarins. Anastomotic intimal hyperplasia: mechanical injury or flow induced. *J Vasc Surg*, 15:708–717, 1992.

[8] M. Bozzetto, B. Ene-Iordache, and A. Remuzzi. Transitional flow in the venous side of patient-specific arteriovenous fistulae for hemodialysis. *Annals of Biomedical Engineering*, 44(8):2388–2401, dec 2015.

[9] A. Brahmbhatt, A. Remuzzi, M. Franzoni, and S. Misra. The molecular mechanisms of hemodialysis vascular access failure. *Kidney International*, 89(2):303–316, feb 2016.

[10] M.J. Brescia, J.E. Cimino, K. Appel, and B.J.Hurwich. Chronic hemodialysis using venipuncture and a surgically created arteriovenous fistula. *New England Journal of Medicine*, 275(20):1089–1092, 1966.

[11] S.P. Broderick, J.G. Houston, and M.T. Walsh. The influence of the instabilities in modelling arteriovenous junction haemodynamics. *Journal of Biomechanics*, 48(13):3591–3598, oct 2015.

[12] K. Van Canneyt, T. Pourchez, S. Eloot, C. Guillame, A. Bonnet, P. Segers, and P. Verdonck. Hemodynamic impact of anastomosis size and angle in side-to-end arteriovenous fistulae: A computer analysis. *The Journal of Vascular Access*, 11(1):52–58, 2010.

[13] E. Colley, J. Carroll, S. Thomas, A. Simmons, and T.J. Barber. Development of a patient-specific fsi model of an arteriovenous fistula. 2016.

[14] J.M. Corpataux. Low-pressure environment and remodelling of the forearm vein in brescia-cimino haemodialysis access. *Nephrology Dialysis Transplantation*, 17(6):1057–1062, 2002.

[15] P.F. Davies. Hemodynamic shear stress and the endothelium in cardiovascular pathophysiology. *Nature Clinical Practice Cardiovascular Medicine*, 6(1):16–26, 2008.

[16] A.M. de Villiers, A.T. McBride, B.D. Reddy, T. Franz, and B.S. Spottiswoode. A validated patient-specific FSI model for vascular access in haemodialysis. *Biomechanics and Modeling in Mechanobiology*, 17(2):479–497, nov 2017.

[17] J.W. Deardorff. A numerical study of three-dimensional turbulent channel flow at large reynolds numbers. *Journal of Fluid Mechanics*, 41(02):453, 1970.

[18] I. Decorato, Z. Kharboutly, C. Legallais, and A.V. Salsac. Numerical study of the influence of wall compliance on the haemodynamics in a patient-specific arteriovenous fistula. *Computer Methods in Biomechanics and Biomedical Engineering*, 14(sup1):121–123, aug 2011.

[19] J.C. Duque, M. Tabbara, L. Martinez, J. Cardona, R.I. Vazquez-Padron, and L.H. Salman. Dialysis arteriovenous fistula failure and angioplasty: Intimal hyperplasia and other causes of access failure. *American Journal of Kidney Diseases*, 69(1):147–151, jan 2017.

[20] B. Ene-Iordache, L. Cattaneo, G. Dubini, and A. Remuzzi. Effect of anastomosis angle on the localization of disturbed flow in 'side-to-end' fistulae for haemodialysis access. *Nephrology Dialysis Transplantation*, 28(4):997–1005, 2012.

[21] B. Ene-Iordache, L. Cattaneo, G. Dubini, and A. Remuzzi. Effect of anastomosis angle on the localization of disturbed flow in 'side-to-end' fistulae for haemodialysis access. *Nephrology Dialysis Transplantation*, 28(4):997–1005, jul 2012.

[22] B. Ene-Iordache, L. Mosconi, G. Remuzzi, and A. Remuzzi. Computational fluid dynamics of a vascular access case for hemodialysis. *Journal of Biomechanical Engineering*, 123(3):284, 2001.

[23] B. Ene-Iordache and A. Remuzzi. Disturbed flow in radial-cephalic arteriovenous fistulae for haemodialysis: low and oscillating shear stress locates the sites of stenosis. *Nephrology Dialysis Transplantation*, 27(1):358–368, jul 2011.

[24] B. Ene-Iordache, C. Semperboni, G. Dubini, and A. Remuzzi. Disturbed flow in a patient-specific arteriovenous fistula for hemodialysis: Multidirectional and reciprocating near-wall flow patterns. *Journal of Biomechanics*, 48(10):2195–2200, jul 2015.

[25] L. Formaggia, A. Quarteroni, and A. Veneziani, editors. *Cardiovascular Mathematics*. Springer Milan, 2009.

[26] E. Hairer and G. Wanner. *Solving Ordinary Differential Equations II*. Springer Berlin Heidelberg, 1991.

[27] H. Haruguchi and S. Teraoka. Intimal hyperplasia and hemodynamic factors in arterial bypass and arteriovenous grafts: a review. *Journal of Artificial Organs*, 6(4):227–235, dec 2003.

[28] Y. He, C.M. Terry, C. Nguyen, S.A. Berceli, Y.T.E. Shiu, and A.K. Cheung. Serial analysis of lumen geometry and hemodynamics in human arteriovenous fistula for hemodialysis using magnetic resonance imaging and computational fluid dynamics. *Journal of Biomechanics*, 46(1):165–169, 2013.

[29] L. Hofstra, D.C.J.J. Bergmans, K.M.L. Leunissen, A.P.G. Hoeks, P.J.E.H.M. Kitslaar, and J.H.M. Tordoir. Prosthetic arteriovenous fistulas and venous anastomotic stenosis: Influence of a high flow velocity on the development of intimal hyperplasia. *Blood Purification*, 14(5):345–349, 1996.

[30] Z. Kharboutly, M. Fenech, J.M. Treutenaere, I. Claude, and C. Legallais. Investigations into the relationship between hemodynamics and vascular alterations in an established arteriovenous fistula. *Medical Engineering & Physics*, 29(9):999–1007, 2007.

[31] K. Konner. The arteriovenous fistula. *Journal of the American Society of Nephrology*, 14(6):1669–1680, 2003.

[32] D.N. Ku, D.P. Giddens, C.K. Zarins, and S. Glagov. Pulsatile flow and atherosclerosis in the human carotid bifurcation. positive correlation between plaque location and low oscillating shear stress. *Arteriosclerosis, Thrombosis, and Vascular Biology*, 5(3):293–302, 1985.

[33] R.M. Lancellotti, C. Vergara, L. Valdettaro, S. Bose, and A. Quarteroni. Large eddy simulations for blood dynamics in realistic stenotic carotids.

International Journal for Numerical Methods in Biomedical Engineering, 33(11):e2868, 2017.

[34] S.W. Lee, L. Antiga, and D.A. Steinman. Correlations among indicators of disturbed flow at the normal carotid bifurcation. *Journal of Biomechanical Engineering*, 131(6):061013, 2009.

[35] J.J.P.M. Leermakers, A.S. Bode, A. Vaidya, F.M. van der Sande, S.M.A.A. Evers, and J.H.M. Tordoir. Cost-effectiveness of vascular access for haemodialysis: Arteriovenous fistulas versus arteriovenous grafts. *Journal of Vascular Surgery*, 57(1):286, 2013.

[36] M.S. Lemson, J.H.M. Tordoir, and P.J.E.H.M. Kitslaar M.J.A.P. Daemen. Intimal hyperplasia in vascular grafts. *Eur J Vasc Endovasc Surg*, 19(4):336–350, 2000.

[37] A.S. Les, S.C. Shadden, C.A. Figueroa, J.M. Park, M.M. Tedesco, R.J. Herfkens, R.L. Dalman, and C.A. Taylor. Quantification of hemodynamics in abdominal aortic aneurysms during rest and exercise using magnetic resonance imaging and computational fluid dynamics. *Annals of Biomedical Engineering*, 38(4):1288–1313, 2010.

[38] A.M. Malek. Hemodynamic shear stress and its role in atherosclerosis. *JAMA*, 282(21):2035, 1999.

[39] F. Nicoud, H.B. Toda, O. Cabrit, S. Bose, and J. Lee. Using singular values to build a subgrid-scale model for large eddy simulations. *Physics of Fluids*, 23(8):085106, 2011.

[40] S.B. Pope. *Turbulent Flows*. Cambridge University Press, 2000.

[41] A. Quarteroni and A. Valli. Numerical approximation of partial different equations. *Springer Publishing Company, Incorporated*, 23, 01 1994.

[42] R. Rogallo. Numerical simulation of turbulent flows. *Annual Review of Fluid Mechanics*, 16(1):99–137, 1984.

[43] E. Sho, H. Nanjo, M. Sho, M. Kobayashi, M. Komatsu, K. Kawamura, C. Xu, C.K. Zarins, and H. Masuda. Arterial enlargement, tortuosity, and intimal thickening in response to sequential exposure to high and low wall shear stress. *Journal of Vascular Surgery*, 39(3):601–612, mar 2004.

[44] S. Sivanesan. Sites of stenosis in AV fistulae for haemodialysis access. *Nephrology Dialysis Transplantation*, 14(1):118–120, jan 1999.

[45] J. Smagorinsky. General circulation experiments with the primitive equations. *Monthly Weather Review*, 91(3):99–164, 1963.

[46] J.V. Soulis, O.P. Lampri, D.K. Fytanidis, and G.D. Giannoglou. Relative residence time and oscillatory shear index of non-newtonian flow models in aorta. In *2011 10th International Workshop on Biomedical Engineering*. IEEE, 2011.

[47] W.E. Stehbens, D.W. Liepsch, A. Poll, and W. Erhardt. Recording of unexpectedly high frequency vibrations of blood vessel walls in experimental arteriovenous fistulae of rabbits using a laser vibrometer. *Biorheology*, 32:631–641, 1995.

[48] M. Sturm, H. Lee, S. Thomas, and T. Barber. The haemodynamic effect of an adjustable band in an arteriovenous fistula. *Computer Methods in Biomechanics and Biomedical Engineering*, 20(9):949–957, may 2017.

[49] T.E. Tezduyar. Stabilized finite element formulations for incompressible flow computations. In *Advances in Applied Mechanics*, pages 1–44. Elsevier, 1991.

[50] Vascular-Access-Work-Group. Clinical practice guidelines for vascular access. *American Journal of Kidney Diseases*, 48:S176–S247, 2006.

[51] C. Vergara, D. Le Van, M. Quadrio, L. Formaggia, and M. Domanin. Large eddy simulations of blood dynamics in abdominal aortic aneurysms. *Medical Engineering & Physics*, 47:38–46, 2017.

MOX Technical Reports, last issues

Dipartimento di Matematica
Politecnico di Milano, Via Bonardi 9 - 20133 Milano (Italy)

50/2018 Gervasio, P.; Quarteroni, A.
The INTERNODES method for non-conforming discretizations of PDEs

46/2018 Riccobelli, D.; Ciarletta, P.
Morpho-elastic model of the tortuous tumour vessels

47/2018 Stefanucci, M.; Sangalli, L.M.; Brutti, P.
PCA-based discrimination of partially observed functional data, with an application to Aneurisk65 dataset

48/2018 Arnone, E.; Azzimonti, L.; Nobile, F.; Sangalli, L.M.
Modeling spatially dependent functional data via regression with di fferential regularization

49/2018 Massi, M.C.; Ieva, F.; Lettieri, E.
Data Mining Application to Healthcare Fraud Detection: A Two-Step Unsupervised Clustering Model for Outlier Detection with Administrative Databases

45/2018 Bernardi, M.S.; Carey, M.; Ramsay, J.O.; Sangalli, L.M.
Modeling spatial anisotropy via regression with partial di fferential regularization

44/2018 Bernardi, M.S.; Sangalli, L.M.
Modelling spatially dependent functional data by spatial regression with differential regularization

42/2018 Antonietti, P.F.; Melas, L.
Algebraic multigrid schemes for high-order discontinuous Galerkin methods

43/2018 Fontana, L.; Masci, C.; Ieva, F.; Paganoni, A.M.
Performing Learning Analytics via Generalized Mixed-Effects Trees

41/2018 Mazzieri, I.; Melas, L.; Smerzini, C.; Stupazzini, M.
The role of near-field ground motion on seismic risk assessment in large urban areas